Thermodynamic Stability of Ni-Fe Nanocrystals

Stefan H. Lohaus*, Michel B. Johnson*, Peter F. Ahnn, Mary Anne White, 3 and Brent Fultz 1 California Institute of Technology, Dept. of Applied Physics and Materials Science, Pasadena, CA 91125, USA 2 Dalhousie University, Clean Technologies Research Institute, Halifax, NS B3H 4R2, Canada 3 Dalhousie University, Dept. of Chemistry, Halifax, NS B3H 4R2, Canada (Dated: October 19, 2023)

The heat capacities of nanocrystalline fcc Ni-Fe, and fcc control materials of the same composition but larger crystallites, were measured from 0.5 - 300 K. The heat capacities were integrated to obtain the enthalpy, entropy, and Gibbs free energy, and to quantify how these thermodynamic functions are altered by nanocrystallinity. From prior measurements of the phonon density of states (DOS), it was found that the heat capacity from 10 - 300 K is dominated by phonons, and the larger heat capacity of the nanocrystalline material below 100 K is attributable to its enhanced phonon DOS below 15 meV. At higher temperatures the nanocrystalline material has an additional contribution to its heat capacity that is consistent with phonon anharmonicity. The total entropy of the nanocrystalline material exceeds that of the bulk material by approximately $0.4\,k_{\rm B}/{\rm atom}$ at 300 K. This is insufficient to overcome the enthalpy of grain boundaries and defects in the nanocrystalline material, making it thermodynamically unstable with respect to the control bulk material. The nanocrystalline material also shows a stronger increase of enthalpy with temperature, further counteracting the entropy and causing its excess Gibbs free energy to decrease only moderately with temperature.

* equal contributors

I. INTRODUCTION

The structure and properties of nanomaterials usually differ significantly from their bulk counterparts, and these differences can be exploited in devices with novel functionalities. For example, as engineered devices become smaller, they become composite nanomaterials with new structures and properties. The nanoscale is often a bridge between atomistic behavior and continuum properties. Thermodynamic questions include how atomic vibrations become heat, and how this affects the Gibbs free energy of a nanomaterial, which determines its thermodynamic stability. How stable or unstable are nanostructures at modest temperatures? To date the Gibbs free energy of nanostructured materials is poorly understood, even though it underlies their stability, and their suitability for service in engineered devices.

Most of the entropy of nanostructured materials is vibrational in origin, although there is some configurational entropy from structural degrees of freedom [1]. Vibrational spectra of nanoparticles have been studied for some time, and the large literature on this subject [2] - [42] is surveyed in section II C below. The vibrational entropy is changed by dynamical degrees of freedom in nanocrystalline structures, and should be of thermodynamic importance to the Gibbs free energy. The usual trend is for the vibrational spectra of a nanomaterial to have more low-energy vibrations than its bulk counterpart, giving larger vibrational amplitudes of atoms in the nanomaterial, and a larger vibrational entropy at a given temperature. This lowers the free energy of nanomaterials at finite temperature, but quantifying the thermodynamic consequences remains a challenge.

Because smaller particles have larger surface-to-volume

ratios and higher internal energy per atom, adding an atom to a small particle is less favorable than adding it to a large one. The "Gibbs-Thomson effect" raises the chemical potential of atoms in small particles (and for nearby atoms in local equilibrium with them). Grain growth occurs when these differences in chemical potential cause a diffusive flux from small particles to large particles. Extra contributions to the enthalpy from elastic fields and internal defects are also expected in many as-synthesized nanomaterials. Sometimes the excess enthalpy of nanomaterials can be measured by heating in a calorimeter to high temperatures, transforming the nanomaterial into a material with larger crystallites [4–8].

Here we report new thermodynamic results from cryogenic calorimetry measurements on a nanocrystalline material and its bulk counterpart with larger crystallites. The results are analyzed to obtain the enthalpy, entropy, and Gibbs free energies, and their difference for the two materials. The fcc Ni-Fe materials are the same as used in previous work to measure the phonon density of states (DOS), enthalpy of defects, magnetic properties, and crystal sizes after high-energy ball milling and annealing [2–4]. By comparing the inelastic neutron scattering to the present calorimetry results, we show that the difference in entropy of nanocrystalline and bulk Ni-Fe is dominated by vibrational entropy, which is large enough to make a substantial contribution to the free energy of the 6 nm nanocrystalline material at 300 K. This entropic stabilization is opposed by the excess enthalpy from grain boundaries and defects. Altogether, the nanocrystalline has an excess Gibbs free energy with respect to the bulk control material at 300 K, making the nanocrystalline material thermodynamically unstable at ambient conditions.

II. THERMODYNAMICS OF NANOPARTICLES

A. Heat Capacity and Free Energy

Equilibrium in a material at a temperature T and ambient pressure p is at the minimum of its Gibbs free energy:

$$G(T) = H_p(T) - TS_p(T) . (1)$$

The enthalpy H_p and the entropy S_p have opposite effects on the value of G and therefore opposite effects on the stability. Both can be determined from the heat capacity, C_p , with the relationships:

$$H_p(T) = H_0 + \int_0^T C_p(T') dT'$$
, (2)

$$S_p(T) = S_0 + \int_0^T \frac{C_p(T')}{T'} dT'$$
 (3)

The thermodynamic stability of a nanomaterial with respect to a bulk control material is determined by the difference ΔG^{n-c} (a positive ΔG^{n-c} makes the nanomaterial unstable with respect to the control material):

$$\Delta G^{\rm n-c}(T) = G^{\rm n}(T) - G^{\rm c}(T) \tag{4}$$

$$= \Delta H_p^{\text{n-c}}(T) - \Delta S_p^{\text{n-c}}(T) , \qquad (5)$$

$$\Delta H_p^{\rm n-c}(T) = \Delta H_0^{\rm n-c} + \int_0^T \Delta C_p^{\rm n-c}(T') dT'$$
, (6)

$$\Delta S_p^{\rm n-c}(T) = \Delta S_0^{\rm n-c} + \int_0^T \frac{\Delta C_p^{\rm n-c}(T')}{T'} dT' .$$
 (7)

Where notation such as $\Delta C_p^{\mathrm{n-c}}$ denotes the difference in heat capacity of the nanocrystalline material and the control bulk material at constant pressure. The larger H_0^{n} of the nanocrystalline material originates from grain boundaries, internal stresses, and defects.

The non-equilibrated nanomaterial cannot access all its degenerate configurational microstates at low temperatures, since it is kinetically trapped in its metabasin. At 0 K the material is in one microstate, corresponding to a specific nanocrystalline configuration [43–45]. According to Boltzmann's definition of entropy, $S = k_{\rm B} \ln \Omega$, where $k_{\rm B}$ is the Boltzmann constant and Ω is the number of accessible microstates, the resulting residual entropy at 0 K is zero because $\Omega = 1$. Therefore $\Delta S_0^{\rm n-c} = 0$, in agreement with the Third Law. An alternative viewpoint of a finite residual configurational entropy at 0 K is presented in section IV A.

B. Internal Energy and Entropy of Nanocrystals

Grain boundaries force atoms into irregular local coordinations, increasing their internal energies. Metals with stronger bonding and higher melting temperatures are generally expected to have grain boundaries with higher energies. From work on a number of grain boundary

structures in fcc metals, the grain boundary energy varies from approximately 0.4 to $1.2 \,\mathrm{J/m^2}$ in the sequence Au, Ag, Al, Pd, Cu, Co, Ni, Pt [46, 47]. For fcc Ni metal, however, grain boundaries between crystals with various orientations have energies that span much of this entire range [48].

High energy ball milling produces non-equilibrium nanomaterials by severe plastic deformation. This process creates microstructural features that contribute to the internal energy, and consequently increase the enthalpy of nanomaterials. Point defects such as vacancies are likely, although they have not been reported. Impurities such as interstitial atoms are introduced during ball milling, and line defects such as dislocations are responsible for some of the low-angle boundaries between crystallites, although their density within the crystals may be low [4–7]. Twin boundaries are also possible [6, 8]. Microstructural features give a distribution of internal energies to the different crystallites of both bcc and fcc phases of Ni-Fe alloys [9]. These microstructural sources of internal energy contribute to H_0 of Eq. 2.

Entropy counteracts the enthalpy to lower the Gibbs free energy, and has configurational, magnetic, electronic and vibrational contributions. During the cryogenic calorimetric measurements, atom mobilities are suppressed, and there are no changes in the atomic configurations. We therefore do not measure differences in the configurational entropy between the nanostructured material and the control samples. The magnetic Curie temperature is approximately 850 K, so only a small amount of magnetic entropy is expected around 300 K, as discussed below. The heat goes primarily into atom vibrations. Vibrational entropy can be determined from the phonon density of states (DOS), $g(\varepsilon)$, as [1, 10–12]

$$S_{\text{vib}}(T) = 3k_{\text{B}} \int_{0}^{T} g(\varepsilon) \left[(1 + n_{\varepsilon,T}) \ln(1 + n_{\varepsilon,T}) - n_{\varepsilon,T} \ln n_{\varepsilon,T} \right] d\varepsilon , \qquad (8)$$

where the Planck occupancy factor is $n_{\varepsilon,T} = (\exp(\varepsilon/T) - 1)^{-1}$.

C. Prior Work on Vibrations in Nanomaterials

From prior work, we know that the phonon DOS of a nanocrystalline material differs from that of bulk materials in three ways. These three features have been found for isolated nanoparticles, and for consolidated nanoparticles with grain boundaries between them. They are found in metals, semiconductors, and insulators, and all three are seen in Fig. 1a. They are:

- 1. An enhancement of $g(\varepsilon)$ at low energies (e.g., below 15 meV in Fig. 1a).
- 2. A general broadening of sharp features in $g(\varepsilon)$ (e.g., at 24 and 33 meV).

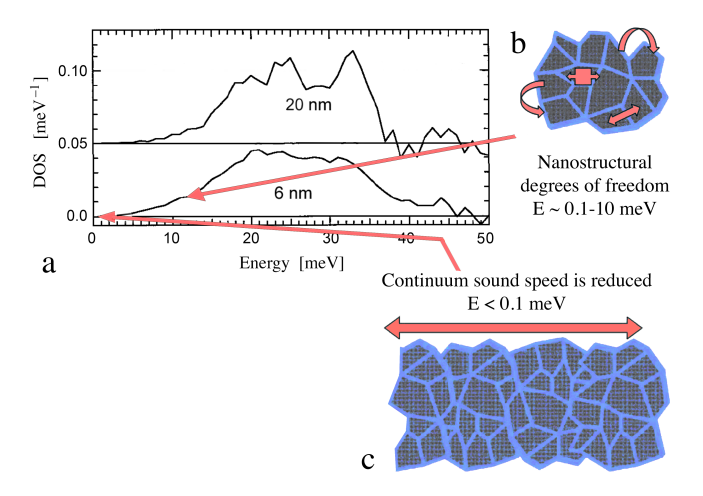


FIG. 1. (a) Phonon DOS from fcc Ni-Fe alloy polycrystalline powder [3]. Compared to the DOS from the material with the larger 20 nm crystallite size, the 6 nm DOS shows: 1 - enhancement of the intensity below 15 meV, 2 - broadening of all features, 3 - a tail of spectral weight above 36 meV. (b) Representative librational or vibrational modes of the nanocrystalline microstructure, with energies of order 1 meV and wavelengths of 10 nm. (c) Continuum behavior at long wavelengths.

3. A tail in $g(\varepsilon)$ that extends to high energies above the usual cutoff frequency of longitudinal phonon modes (e.g., 38-39 meV).

Feature 1 is understood best. An enhancement of $g(\varepsilon)$ at low energies is expected from the degrees of freedom in a nanostructure, as depicted in Fig. 1b. Modes of the nanostructure may originate with the vibrations of nanocrystals against each other, mutual rotations, or with the partial confinement of vibrational waves to boundary regions, similar to Rayleigh waves at surfaces with elastic discontinuities. This enhancement disappears at very low energies when the wavelengths are longer than the nanostructural features (Fig. 1c), so the material behaves as a continuum with altered elastic constants [50–56].

Both calculations and measurements on either isolated nanocrystals or nanocrystals with rigid constraints showed an enhancement of modes at low energies [13–42]. This low-energy regime sometimes indicates a change in the dimensionality of the vibrational modes. Fitting the low-energy part of $g(\varepsilon)$ to ε^n has given n < 2, i.e., smaller than for three-dimensional vibrations [23, 25, 39]. This exponent n can be close to 1.0 as expected for two-dimensional vibrations [22, 32, 49]. This is not a universal result, however, and often $n \simeq 2$ in consolidated nanocrystals [3, 29]. Nevertheless, more modes are found at low energies, sometimes by a factor of five or so [3, 18, 20, 21, 24, 29, 32, 35, 36, 38, 39]. Transferring phonon spectral weight from higher energies to lower energies causes an increase in the vibrational entropy as calculated by Eq. 8, because the Planck factor, $n_{\varepsilon,T}$, is largest at low ε .

Feature 2, the broadening of features in the $g(\varepsilon)$ of nanomaterials, is less understood. This broadening has been attributed to the shortening of phonon lifetimes, which could explain both features 2 and 3 [21]. In a crystal smaller than 10 nm, a phonon propagates only tens of atomic distances before it encounters a surface or grain boundary. If the phonon is scattered at the interface by effects of disorder or anharmonicity, its lifetime may be only tens of vibrational periods or less. The spectral shape of a damped harmonic oscillator function has an asymmetrical broadening about the central frequency that can often account for the broadened phonon DOS of nanostructured materials [2, 3, 21, 31–35, 40, 41, 57]. Phonon lifetime broadening in nanomaterials is controversial, however. Some prior work indicated that these tails originate from harmonic modes at high frequencies caused by surface oxides or impurities [26, 32, 36, 38, 42]. High energy tails of the phonon DOS have also been reported in a number of molecular dynamics simulations on pure materials [19, 23, 27, 30, 38], and have been attributed to higher frequency harmonic vibrations of atoms at surfaces of nanoparticles.

III. EXPERIMENTAL METHODS AND RESULTS

A. Materials

Inelastic neutron scattering measurements of phonon densities of states typically require several grams of material. High energy ball milling has proved practical for preparing materials with small crystals. These crystals are consolidated into larger particles of powder. The relatively low surface areas of the powders make them less prone to adsorption of gases and water, which would impede neutron scattering measurements. Powders from previous neutron scattering work [2-4] were sealed and stored for 20 years, and some calorimetry measurements were performed on them. The x-ray diffraction (XRD) patterns of the materials were unchanged after the time of storage. There was no evidence of new oxide, and the widths of their fcc diffraction peaks were unchanged. In prior work, these powders were well characterized by inelastic neutron scattering, small-angle neutron scattering, transmission electron microscopy, x-ray diffractometry (XRD), Mössbauer spectrometry, and magnetic susceptibility [2–4].

To prepare new samples by a similar method, powders of Ni (75 atomic%) and Fe (25 atomic%) were mixed with 5 wt.% stearic acid or ethanol and sealed in a steel vial. Ball milling was performed with a Fritsch Planetary Mono Mill for 20 h at 650 rpm using steel ball-to-powder weight ratios between 20:1 and 40:1. After milling, the material was sonicated in isopropyl alcohol and centrifuged to remove the stearic acid. We call the nanomaterials prepared by high energy ball milling "asmilled" samples. Control samples of bulk material can

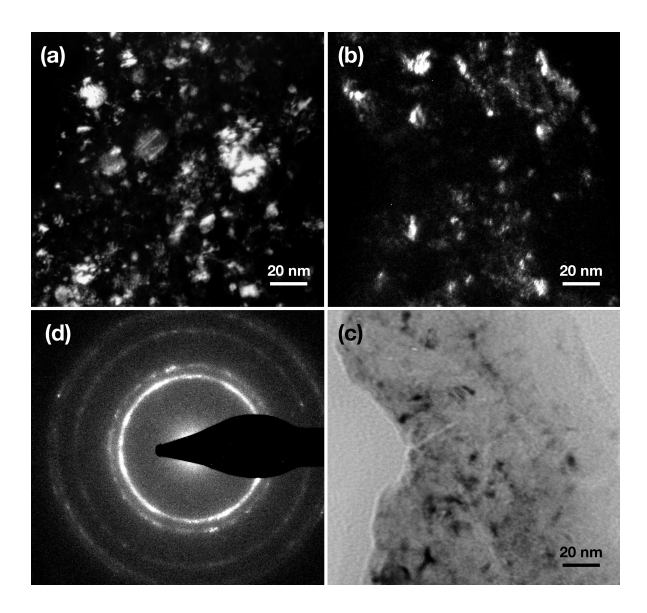


FIG. 2. Transmission electron microscopy images of the asmilled Ni-Fe. The dark-field (DF) and bright-field (BF) images were obtained with the (111) fcc diffraction. (a) DF image of old sample [3], (b) DF image of new sample, (c) BF image of new sample, (d) electron diffraction pattern.

be prepared by milling the powder for shorter times, by milling with a lower ball-to-powder ratio or by annealing the as-milled material in sealed quartz ampoules under vacuum.

Transmission electron microscopy (TEM) images were obtained from the old and new nanocrystalline samples. The dark-field and bright-field TEM images presented in Fig. 2 show the grain sizes of the as-milled samples, and are direct evidence of their nanocrystallinity. The mean crystallite size of the nanomaterial was determined to be 6 nm [3].

XRD patterns using Cu K_{α} radiation were acquired for all materials. Figure 3 shows the XRD patterns obtained from the new and old samples in the as-milled state, and after annealing at 873 K for 1 h. The diffraction data show main peaks from an fcc solid solution, but some distortions and small peaks are evident in the diffraction pattern that are probably from NiO. The widths of the fcc diffraction peaks of the as-milled material are very similar to the older samples used in the previous work. We estimated a grain size of 25 - 30 nm for the annealed powder, by comparing the widths of its XRD peaks with the nanomaterial.

There is evidence for some L1₂ chemical order (where the Fe atoms occupy the corners and the Ni atoms the faces of the standard fcc cube) in a few of the annealed control samples, but this should not alter the phonon DOS significantly [58–60]. Other control samples did not show this L1₂ chemical order and all control samples gave very similar curves of $C_p(T)$ as shown in Fig. 4.

To measure the concentration of impurities, the asmilled and annealed control samples were sent to a

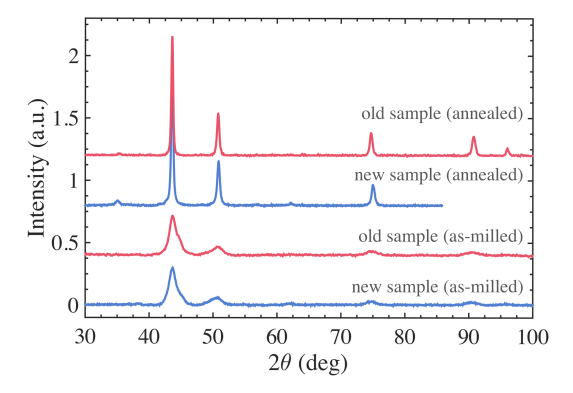


FIG. 3. X-ray diffraction patterns from new and old as-milled Ni-Fe powders, and after annealing them at 873 K for 1 h.

commercial laboratory for an instrumental gas analysis (IGA). In this method, the concentration of gas-forming elements (C, O, N and S) is measured by rapidly heating the sample above 2000°C in an inert environment. These elements are released as gases, that are measured by infrared and thermal conductivity detectors. Results are shown in Table I.

Element	Nanomaterial (wt%)	Control (wt%)
О	2.8	2.4
С	1.7	1.6
N	0.0064	0.0063
S	0.0018	0.0034

TABLE I. IGA measurements on the as-milled nanomaterial, and the control sample prepared by annealing the as-milled material, showing the concentration of impurities.

B. Heat Capacity

Specific heat measurements were made by relaxation microcalorimetry using a commercial instrument, a Physical Property Measurement System (PPMS, from Quantum Design, San Diego). Measurements were conducted in the temperature range between 0.5 and 300 K over which accuracy, with due care, can be within 1% from 5 K to 300 K, and 5% from 0.4 K to 5 K [72]. Measurements were takes in two modes: ⁴He cooling for the 2 to 300 K temperature interval and ³He cooling for the interval from 0.5 to 10 K. To enhance the thermal contact between the sample and the microcalorimeter, a thin layer of Apiezon N grease was applied to the sample stage and its contribution to the specific heat is accounted for during addendum measurements prior to each sample measurement. All measurements were conducted under high vacuum (10^{-5} Torr) to minimize convective heat losses.

For the relaxation calorimetry measurements, the asmilled powder samples were consolidated into pellets using a 0.28 cm diameter die. An appropriate amount of powder was added to the die and hydraulically pressed

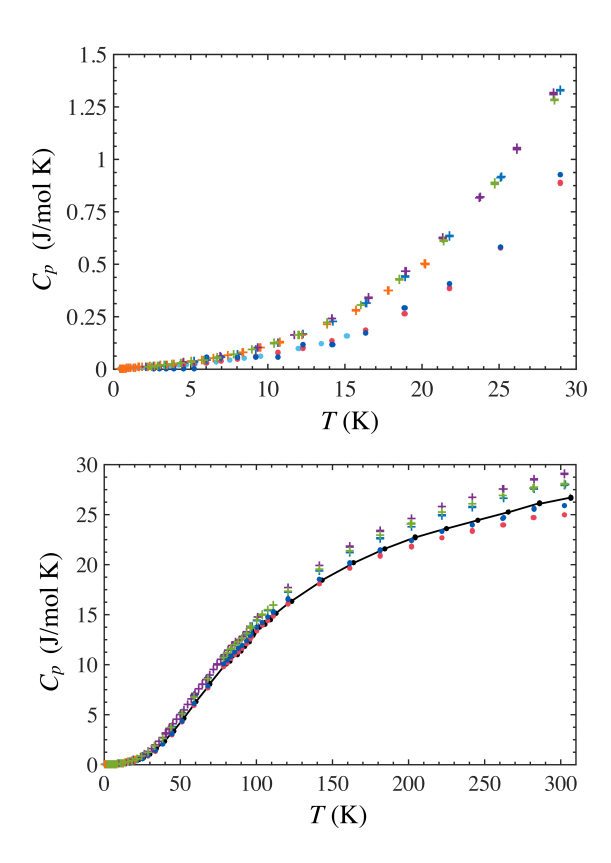


FIG. 4. Heat capacities of the Ni-Fe materials (normalized by the number of moles of atoms). Top curves with + symbols are from as-milled 6 nm materials; bottom curves with o symbols are from large-grained control samples. Different symbol colors represent results from different samples. (a) Low-temperature region. (b) Full data sets. The solid black line is from the annealed nanocrystalline material (see text).

with a force of 2700 N, resulting in a pressure of approximately $0.45\,\mathrm{GPa}$. The consolidated samples had better thermal contact and heat transfer, and allowed for more accurate mass determinations owing to ease of handling without sample loss during transfers. The mass of each pellet was measured (Sartorius semi-micro balance), and the pellet was transferred onto the sample stage and lightly pressed into the grease film. The sample masses ranged from 10 to 27 mg.

Several heat capacity measurements were performed on nanocrystalline (as-milled) and control samples (less milled or annealed). The results are shown in Fig. 4. There are some variations between samples of each type, but in all cases the heat capacity curves for the nanocrystalline material exceeded the heat capacity of the control samples. This difference was most evident at low temperatures, as expected owing to the enhanced phonon DOS at low energies.

The heat capacity of the as-milled nanocrystalline material was also enhanced at temperatures above 200 K. We were concerned that this could be from interstitial impurities, carbon and oxygen, that were introduced into the material by milling. This motivated the preparation

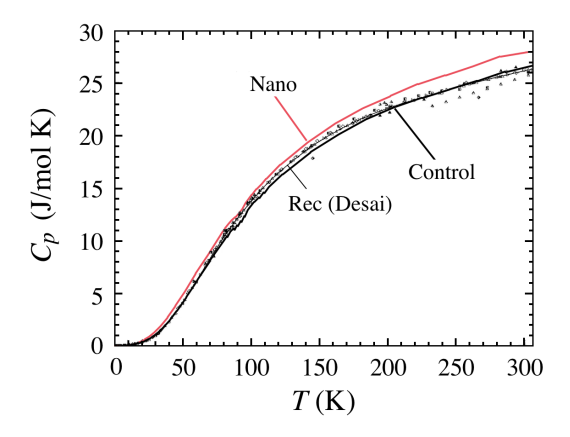


FIG. 5. Representative heat capacity of as-milled nanocrystalline Ni-Fe (red) and the same material after annealing at 873 K (control), compared to data compiled by Desai for fcc Ni as small markers, including the recommended curve as a thin solid line [73].

of control samples by annealing the as-milled material at 873 K to increase the crystallite size and eliminate defects. The intent was to obtain a bulk control sample with the same interstitial atoms as the nanomaterial, and this was successful, as shown in the IGA results (Table I). The heat capacity of this annealed control sample, shown in Fig. 4 as a solid line, is similar to that of the other samples of Ni-Fe with large crystals, however, showing that the enhanced heat capacity above 200 K does not originate from interstitial impurities.

Our measured heat capacity for the control sample is similar to the heat capacity measured on fcc Ni [73], as shown in Fig. 5. Low temperature measurements on disordered Ni₃Fe [74] are in excellent agreement with the heat capacity of our control sample. A study of Ni₃Fe at high temperatures gave a heat capacity of 25.5 J/(mol K) at 300 K [59], in the bottom part of the range for Ni in Fig. 5. Full L1₂ ordering transition in this material reduces the heat capacity by approximately $0.1\,k_{\rm B}/{\rm atom}$ [59], with most of this from phonons [60]. The L1₂ ordering in Ni₃Fe is sluggish. It is a first-order transition, so with partial order, the change in heat capacity would be reduced proportionately.

For our control sample prepared by annealing the asmilled powder, the linear temperature dependence of the heat capacity below 2.5 K (see Fig. 6) gave the slope $\gamma{=}4.3\,\mathrm{mJ/(mol~K^2)},$ in excellent agreement with the value of 4.178 mJ/(mol K²) for disordered Ni₃Fe reported by Kollie, et al. [74]. For our nanocrystalline material, $\gamma{=}5.9\,\mathrm{mJ/(mol~K^2)}.$ At 300 K, the resulting difference in electronic heat capacity ($C_p^{\rm el}=\gamma T$) between the nanocrystalline and control samples is predicted to be small, $0.06\,k_{\rm B}/\mathrm{atom}$ (0.47 J/(mol K)) .

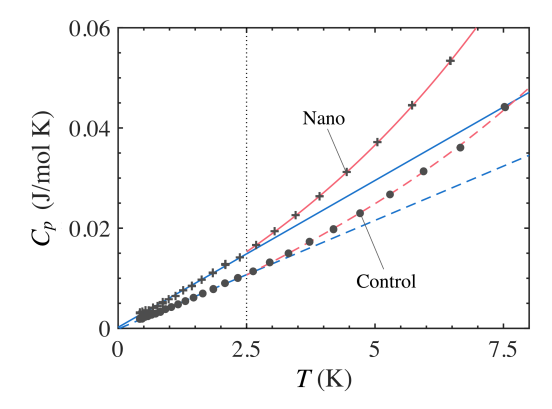


FIG. 6. Low temperature heat capacities of the nanocrystalline and control materials. Linear fits bellow 2.5 K (blue lines) correspond to electronic contributions $C_p^{\rm el} = \gamma T$. Red curves are fits using the Debye model above 2.5 K, corresponding to the phononic contribution at low temperatures $(C_p^{\rm ph} \propto T^3)$.

C. Defect Recovery and Grain Growth

Differential Scanning Calorimetry (DSC) was performed using a Perkin Elmer DSC 7 to quantify the internal enthalpy difference $\Delta H_0^{\rm n-c}$ of Eq. 6, associated with defects and grain boundaries. Samples from an asmilled nanomaterial with grain sizes of 7 nm were placed in crucibles (either alumina or annealed aluminum pans) in the DSC sample holder with a purge gas flow of N_2 at 20- $30\,\mathrm{ml/min}$. The differential heat flow to the sample was measured while heating it from $320\,\mathrm{K}$ to $873\,\mathrm{K}$ at $20\,\mathrm{K/min}$.

The heat evolution measured by DSC is shown in Fig. 7. The defect recovery and grain growth are exothermic and irreversible processes, so subsequent DSC runs on the same sample lack the exothermic peak between 580 - 800 K, indicating that the entire recovery occurred during the first run. The difference in heat flow between the first and second runs shown in Fig. 7 corresponds to the difference between the nanomaterial and the control sample with larger grains. To quantify the enthalpy of defects and grain growth, a linear baseline was used to calculate the area of the highlighted exothermic peak. The resulting enthalpy of defect recovery and grain growth $H_0^{\rm n-c} = 3.9^{+0.2}_{-1.0}\,{\rm kJ/mol.}$ (Polynomial baselines give lower enthalpy values, hence the larger lower bound).

We showed that the highlighted exothermic peak of Fig. 7 corresponds to grain growth of the nanocrystalline material by heating the as-milled material in vacuum to different temperatures at $20\,\mathrm{K/min}$ and acquiring XRD patterns after cooling. The grain sizes, calculated from the widths of the XRD peaks, are included in Fig. 7. The XRD patterns, presented in the Supplemental Material, showed sharpening of the diffraction peaks with increasing annealing temperatures and showed that most of the grain growth during heating occurs indeed between 580

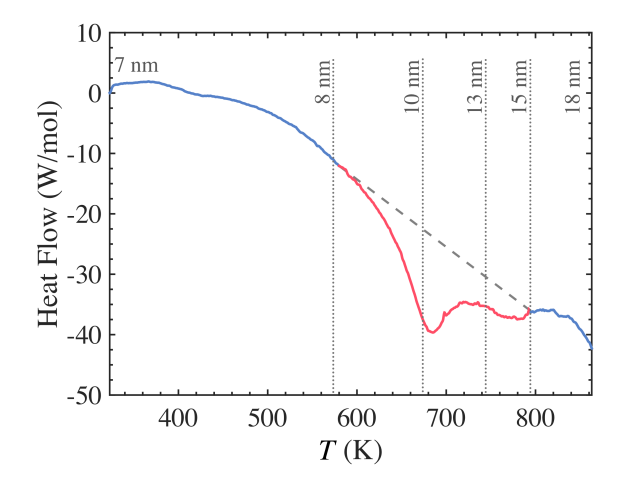


FIG. 7. Difference of the heat flow between the first and second runs measured by DSC. Positive values correspond to endothermic heat flows. The release of internal energy from defects and grain growth is highlighted (red) and its enthalpy was calculated using a linear baseline (dashed line). The labeled grain sizes were determined from measured XRD patterns presented in the Supplemental Material.

and $800 \,\mathrm{K}$.

D. Phonon Density of States

The vibrational contribution to the heat capacity was obtained from the phonon DOS, $g(\varepsilon)$ as [1, 10]

$$C_p(T) = 3N k_{\rm B} \int_0^\infty g(\varepsilon) \left(\frac{\varepsilon}{k_{\rm B}T}\right)^2 \times \frac{e^{\varepsilon/k_{\rm B}T}}{\left(e^{\varepsilon/k_{\rm B}T} - 1\right)^2} d\varepsilon . \quad (9)$$

where ε is the phonon energy. In Eq. 9, the phonon DOS, $g(\varepsilon)$, is normalized to 1, and N is the number of atoms in the sample.

Figure 8a shows phonon DOS curves from prior work, measured by inelastic neutron scattering, and a solid curve calculated with a Born–von Kármán model. These curves were used with Eq. 8 to calculate the phonon contribution to the entropy (Fig. 8b), and with Eq. 9 to obtain the heat capacity originating from phonons (shown in Fig. 9 for the 6 nm, 50 nm and calculated (Calc) curves). We considered that the low energy part of the 50 nm sample may be low, owing to sampling of the phonon spectra with restricted range of momentum transfer in the triple-axis measurements of [4], but such an error had only a small effect on the phonon entropy and heat capacity.

A quick comparison of Fig. 8b with the entropy computed from the heat capacity measurements (Fig. 11b) shows that most of the entropy is from phonons. Figure 9 also shows that approximately 90% of the heat capac-

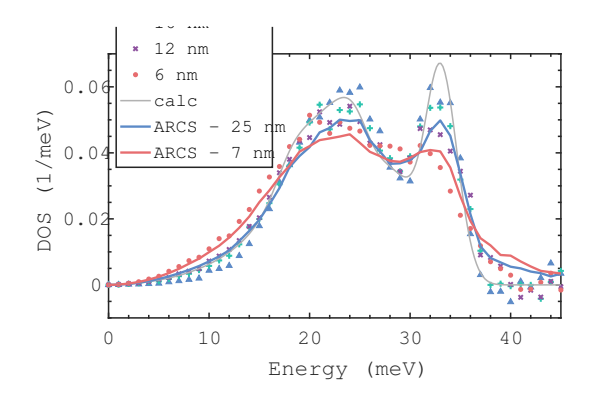


FIG. 8. (a) Phonon DOS curves measured previously on nanocrystalline Ni-Fe before and after annealing to prepare larger crystallites of approximately the mean size as labeled [4]. Solid black curve (Calc) was calculated with a Born–von Kármán model using force constants from [58], and broadened by instrument resolution. (b) Phonon entropies calculated with the curves of panel a, using Eq. 8.

ity of the Ni-Fe material is from phonons. The increase of heat capacity above the classical limit of $24.94\,\mathrm{kJ/mol}$ ($3\,k_\mathrm{B}/\mathrm{atom}$) requires more than harmonic or quasiharmonic phonons, which predict a heat capacity of $3\,k_\mathrm{B}$ per atom at high temperatures.

In what follows, we show that adding the contributions from electrons and spins to the phonon entropy contribution of Fig. 8b brings the heat capacity of the control material into better agreement with results from calorimetry. These extra contributions are small, however, and do not differ significantly between the nanocrystalline and control materials.

IV. DISCUSSION

A. Residual Entropy at 0 K

The configurational degrees of freedom of the nanomaterial are not equilibrated, and are unchanged between 0 K and approximately 580 K, when the heat evolution from defect annihilation and grain growth is observed. This heat evolution shown in Fig. 7 can be integrated to give $0.7\,k_{\rm B}/{\rm atom}$, which could be used as a residual entropy at 0 K. However, the configuration of the nanocrystalline material is frozen below 580 K, so this residual entropy does not contribute to the free energy because it has no ability to do work. Furthermore, all of the heat capacity below 300 K is accounted for by phonons, electrons and magnetism (as discussed below with Fig. 10), and an additional $0.7\,k_{\rm B}/{\rm atom}$ is well outside the errors of measurement.

A residual entropy calculated with $\Delta S = \int C_p/T dT$ assumes an equilibrated system, which is not the case for the configurational degrees of freedom. Even though many possible configurations are thermodynamically allowed, corresponding to a high degree of degeneracy, the

nanomaterial is kinetically trapped. It can access only its own metastable basin, which at 0 K consists of a single microstate [43–45]. Boltzmann's entropy definition, $S = k_{\rm B} \ln \Omega$, which is consistent with the 2nd Law of thermodynamics for non-equilibrated systems [76], gives $S_0^n = 0$ for the configurational degrees of freedom of our nanocrystalline material when $\Omega = 1$.

B. Electronic and Magnetic Contributions to the Heat Capacity

The electronic contribution to the heat capacity, $C_p^{\rm el} = \gamma T$, can be determined from the total heat capacity measurements below 2.5 K. At these temperatures, the electronic heat capacity exceeds that of phonons, which follows a T^3 behavior as in the Debye model [75]. Fig. 6 shows the low temperature part of the heat capacity data of Fig. 4, together with the individual contributions from electron and phonons. We obtain a value of $\gamma = 5.9 \, {\rm mJ/(mol~K^2)}$ for our nanocrystalline material and $\gamma = 4.3 \, {\rm mJ/(mol~K^2)}$ for the bulk control sample.

Results from calculations have been reported for the electronic heat capacity of fcc Ni, and the fcc alloys Ni₇₀Fe₃₀ and Ni₅₀Fe₅₀, sometimes with comparisons to experimental calorimetric data. At 300 K, the electronic plus magnetic heat capacity has been reported to be 0.25 [61], 0.23 [62], 0.16 [63] $k_{\rm B}/{\rm atom}$, values that are slightly larger than the electronic heat capacity of $C_p^{\rm el} = \gamma T = 0.16 \ k_{\rm B}/{\rm atom}$ that we obtain for our bulk material. Our nanocrystalline material has a $C_p^{\rm el} = 0.22 \ k_{\rm B}/{\rm atom}$ at 300 K.

Experimental measurements show only a small decrease in lattice magnetization with temperature for Ni around 300 K [64], but measurements on nanocrystalline Ni have shown a suppression of the Curie temperature by approximately 100 K, and a more rapid decrease of lattice magnetization near 300 K [65–68]. There may be a systematic decrease in Curie temperature with the inverse of grain size in Ni [67], but the decrease in magnetization with temperature is not understood systematically for nanocrystals. A magnetic contribution would increase rapidly at the upper end of our temperature range, however, and would not be so monotonic as the difference in heat capacity seen in Fig. 9 between the nano and control samples. Although the temperature dependence of the magnetic order of ball milled Ni-Fe was not measured in the present work, the magnetic permeability at room temperature was shown to be somewhat higher than the control sample [4]. It is possible that there is more thermal magnetic disorder in the nanocrystalline material than the control sample. A plausible upper bound for the excess magnetic heat capacity of the nanomaterial at $300 \,\mathrm{K}$ is $0.1 \,k_{\mathrm{B}}/\mathrm{atom}$. The total magnetic contribution to the heat capacity at 300 K given by Körmann, et al., for fcc bulk Ni is $0.1 k_{\rm B}/{\rm atom}$ [61].

We calculated possible effects of interstitial impurities on the heat capacity, assuming they contributed to

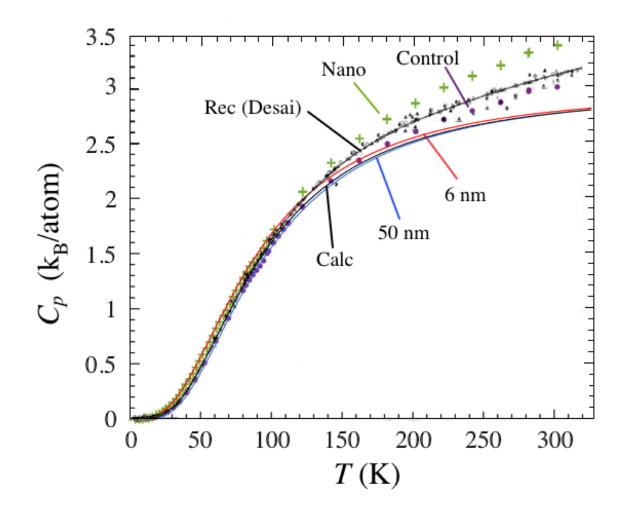


FIG. 9. Superposition of heat capacities from calorimetry shown in Fig. 5, with heat capacities calculated from three phonon DOS curves as labeled in Fig. 8a, using Eq. 9.

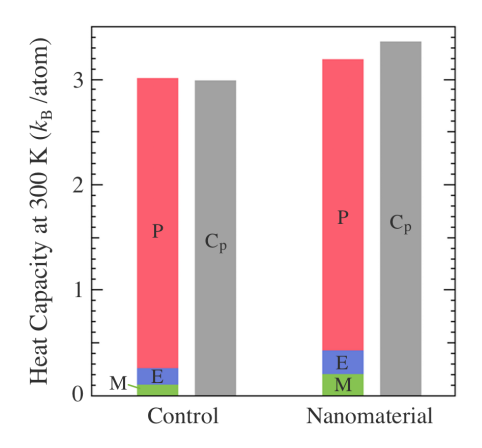


FIG. 10. Individual contributions to the heat capacity at $300\,\mathrm{K}$ of the control and nanocrystalline samples from magnetization (M), electrons (E) and phonons (P) compared to the total heat capacity measured by calorimetry (C_{p}) .

Einstein-type vibrational modes towards the top of the phonon DOS (at 50 meV or somewhat higher, for example). These calculations were performed by reducing the mole fraction of Ni₃Fe to accommodate the interstitial atoms, keeping the same total mass of the sample, and using a concentration of interstitial atoms consistent with the IGA measurement of Table I. To summarize this analysis, we found that if the heat capacity at 300 K was accounted for by modes of these interstitials, the reduced number of Ni and Fe atoms caused a suppression of the heat capacity at temperatures below 150 K, opposite to the experimental observations. Less than $0.1\,k_{\rm B}/{\rm atom}$ could be contributed to the heat capacity at 300 K owing to the differences in impurity concentrations of the nanocrystalline and control samples.

C. Contributions to the Heat Capacity from Anharmonicity and Thermal Expansion

It is straightforward to calculate the contribution to the heat capacity from thermal expansion

$$\Delta C_p^{\text{te}}(T) = \frac{1}{2} B v \beta^2 T \ . \tag{10}$$

Using a bulk modulus of 182 GPa, molar volume of $6.59\,\mathrm{cm}^3/\mathrm{mol}$, volume thermal expansion of $3.9\times10^{-5}/\mathrm{K}$ (a value at 300 K; the thermal average is lower), we get $\Delta C_p^{\mathrm{te}} = 0.27\,\mathrm{J/(mol~K)}$, which is less than 1% of the heat capacity at 300 K.

The contributions to the heat capacity at $300 \,\mathrm{K}$ are shown graphically in Fig. 10. In principle, the sum of these individual contributions should equal the heat capacity C_p measured by calorimetry. This is quite satisfactory for the control sample, but the measured heat capacity of the nanocrystalline material is larger than the sum of the individual contributions, even when accounting for the uncertainty in each quantity.

A possible explanation is that the phonon DOS of the nanocrystalline material is broadened by shortened phonon lifetimes, not by a distribution of harmonic modes. (This anharmonic effect is not accounted for in Eq. 8 and 9, and therefore does not appear in the phonon contribution to the heat capacity "P" in Fig. 10. It is also missing from the calculated heat capacities of Fig. 9.) Lifetime broadening tends to shift spectral weight to higher energies, giving an apparent reduction in the entropy when calculated with Eq. 8. A correction for this effect, given in Ref. [69], predicts an increase in phonon entropy of $0.2 k_{\rm B}/{\rm atom}$ for a damped harmonic oscillator with a quality factor, Q, of 4 or 5, which is consistent with the broadened phonon DOS of the nanocrystalline Ni-Fe. Shortened phonon lifetimes account well for the lower value of the sum of the contributions of Fig. 10 compared to " C_p " and are, therefore, consistent with our experimental observations. Unfortunately, identifying anharmonic contributions to the heat capacity is not straightforward. An anharmonic contribution of a fraction of one $k_{\rm B}/{\rm atom}$ is typical for metals at high temperatures [77], however.

D. Gibbs Free Energy

The H_0 term in Eq. 2 is an important contribution to the enthalpy of the nanocrystalline material. It was measured by the heat evolved when the nanocrystalline material was heated to 873 K (approximately half the melting temperature of bulk material), as the grains grew and the defects were annihilated. Making a semiquantitative estimate, the measured 3.9 kJ/mol of heat release from defect recovery corresponds to a surface energy of $1.2\,\mathrm{J/m^2}$ if the crystallites were 6 nm cubes. The enthalpy $H_p(T)$ was obtained by integrating the heat capacity as in Eq. 2, and it is shown in Fig. 11a. The difference of

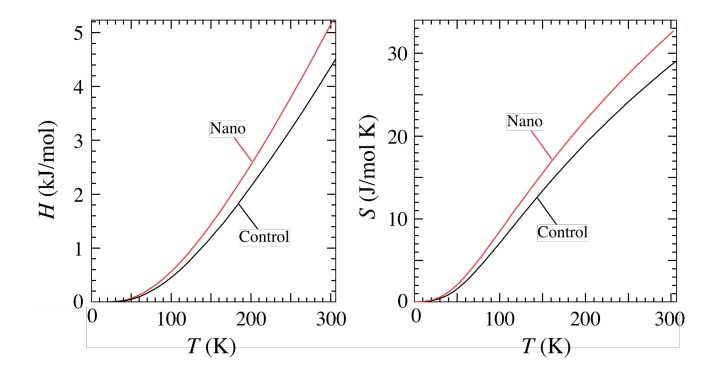


FIG. 11. (a) Enthalpy and (b) Entropy of nanocrystalline material and control sample after annealing computed from heat capacity measurements using eq. 2 and 3. The grain boundary enthalpy H_0 is not included.

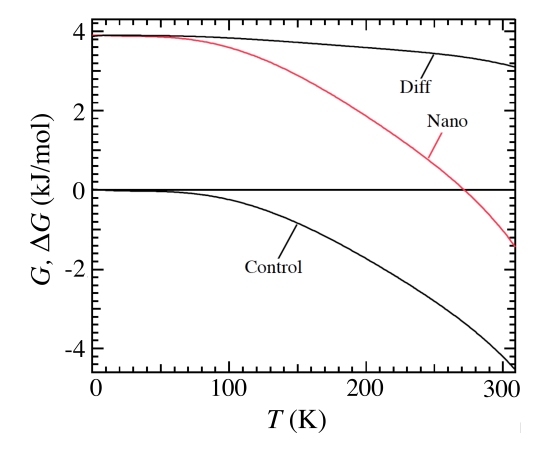


FIG. 12. Gibbs free energy of as-milled nanocrystalline Ni-Fe and control sample after annealing at 873 K, using enthalpy and entropy of Fig. 11, and $\Delta H_0^{\rm n-c} = 3.9\,{\rm kJ/mole}$.

 $H_p(T)$ between the nanocrystalline and control material, $\Delta H_n^{\rm n-c}(T)$, increases with temperature.

The entropy of formation of a grain boundary is positive, helping to stabilize a consolidated nanomaterial at finite temperatures by Eq. 1. The excess entropy obtained from calorimetry at 300 K is 0.4 k_B/atom (3.5 J/mol K). An early report gave a far larger total entropy [50]. Isolated iron nanoparticles also showed a large increase of phonon entropy of $0.5 k_{\rm B}/{\rm atom}$ [8]. Our measured value of $\Delta S^{\rm n-c} = 3.5 \, \text{J/mol K}$ contributes to the Gibbs free energy with $-T\Delta S = -1.1 \,\mathrm{kJ/mol}$ at 300 K, and this should be larger at 600 K where the grain growth starts, perhaps as large as $-2.5 \,\mathrm{kJ/mol}$. This higher entropy of the nanomaterial at 600 K would still be insufficient to overcome the enthalpy of its grain boundaries (3.9 kJ/mol). Since diffusion is thermally activated, the grains start to grow at 600 K, transforming the unstable nanomaterial into its stable counterpart with larger crystallites.

Figure 12 shows that the excess Gibbs free energy $\Delta G^{\rm n-c}(T)$ (labeled "Diff") is positive at all tempera-

tures. The nanocrystalline material has a larger entropy, and a larger enthalpy, than the control sample. The net effect is to reduce the $\Delta G^{n-c}(T)$ with temperature somewhat, but not enough to overcome the enthalpy H_0 from grain boundaries and defects in the nanocrystalline material.

V. CONCLUSIONS

The heat capacities of nanocrystalline and largegrained fcc Ni-Fe alloys were measured from 0.5 - 300 K. The heat capacity of the nanocrystalline material was consistently larger, especially at temperatures below 100 K. This difference originates from its larger phonon density of states (DOS) at energies below 15 meV, known from prior inelastic neutron scattering. The phonon DOS curves accounted for most of the heat capacities of the Ni-Fe samples, and for most of the difference between the nanocrystalline and control samples. Adding electronic and magnetic contributions to the vibrational heat capacity gave a total heat capacity of the control sample to an accuracy of 2%, approximately the uncertainty from the experimental techniques. Adding all components of the heat capacity of the nanocrystalline material gave a result that was about 6% lower than the measured heat capacity at 300 K. This difference is attributed to a larger phonon anharmonicity in the nanocrystalline material, which could also cause the large broadening of features in its phonon spectrum. The larger entropy of the nanocrystalline material with respect to the control sample is counteracted by its larger enthalpy, so the difference in Gibbs free energy between the nanocrystalline and control sample decreases only modestly with temperature. The nanocrystalline material is thermodynamically unstable at temperatures to 300 K, and is probably unstable to higher temperatures where grain growth occurs.

VI. ACKNOWLEDGEMENT

This work was supported by the Department of Energy through the Basic Energy Sciences Grant DE-FG02-03ER46055. MAW acknowledges support from NSERC (Grant number RGPIN-2015-04593), the Canada Foundation for Innovation, and the Clean Technologies Research Institute at Dalhousie University.

- [1] B. Fultz, *Phase Transitions in Materials* (Cambridge University Press, 2014).
- [2] H.N. Frase, L.J. Nagel, J.L. Robertson, and B. Fultz, Philos. Mag. B 75, 335 (1995).
- [3] H.N. Frase, B. Fultz, and J.L. Robertson, Phys. Rev. B 57, 898 (1998).
- [4] H.N. Frase, Ph.D. thesis in Materials Science, California Institute of Technology (April 9, 1998). Download at https://thesis.library.caltech.edu/301/
- [5] H.J. Fecht, Nanostructured Materials 6, 33 (1995).
- [6] O. Boytsov, A.I.. Ustinov, E. Gaffet, F. Bernard, J. Alloys Compounds 432, 103 (1998).
- [7] J.Y. Huang, Y.K Wu, H.Q. Ye, Microscopy Res. Technique 40, 101 (1998).
- [8] B. Roldan Cuenya, L.K. Ono, J.R. Croy, et al., Phys. Rev. B 86, 165406 (2012).
- [9] L.B. Hong and B. Fultz, J. Appl. Phys. 79, 3946 (1996).
- [10] D.C. Wallace, Thermodynamics of Crystals (Dover, Mineola, New York, 1998).
- [11] A. van de Walle and G. Ceder, Revs. Mod. Phys. 74, 11 (2002).
- [12] B. Fultz, Prog. Mater. Sci. **55**, 247 (2010).
- [13] W. Damgaard Kristensen, E.J. Jensen, and R.M.J. Cotterill, J. Chem. Phys. 60, 4161 (1974).
- [14] A. Tamura, K. Higeta, and T. Ichinokawa, J. Phys. C 15, 4975 (1982).
- [15] A. Tamura, K. Higeta, and T. Ichinokawa, J. Phys. C 16, 1585 (1983).
- [16] K. Suzuki and K. Sumiyama, Mater. Trans. JIM 36, 188 (1995).
- [17] B. Fultz, L. Anthony, L.J. Nagel, et al., Phys. Rev. B 52, 3315 (1995).
- [18] J. Trampenau, K. Bauszus, W. Petry, and U. Herr, J. Nanostruct. Mater. 6, 551 (1995).
- [19] D. Wolf, J. Wang, S.R. Phillpot, and H. Gleiter Phys. Rev. Lett. 74, 4686 (1995).
- [20] B. Fultz, J.L. Robertson, T.A. Stephens, et al., J. Appl. Phys. 79, 8318 (1996).
- [21] B. Fultz, C.C. Ahn, E.E. Alp, et al., Phys. Rev. Lett. 79, 937 (1997).
- [22] U. Stuhr, H. Wipf, K.H. Andersen, and H. Hahn, Phys. Rev. Lett. 81, 1449 (1998).
- [23] A. Kara and T.S. Rahman, Phys. Rev. Lett. 81, 1453 (1998).
- [24] E. Bonetti, L. Pasquini, E. Sampaolesi, et al., J. Appl. Phys. 88, 4571 (2000).
- [25] P. Derlet, R. Meyer, L.J. Lewis, et al., Phys. Rev. Lett. 87, 205501 (2001).
- [26] L. Pasquini, A. Barla, A.I. Chumakov, et al., Phys. Rev. B 66, 73410 (2002).
- [27] R. Meyer, S. Prakash, P. Entel, Phase Transitions **75**, 51 (2002).
- [28] R. Meyer, L.J. Lewis, S. Prakash, and P. Entel, Phys. Rev. B 68, 104303 (2003).

- [29] A.B. Papandrew, A.F. Yue, B. Fultz, I. Halevy, et al., Phys. Rev. B 69, 144301 (2004).
- [30] A. Kara, A.N. Al-Rawi, and T.S. Rahman, J. Comp. Theor. Nanoscience 1, 216 (2004).
- [31] P. Machnikowski and L. Jacak Phys. Rev. B 71, 115309 (2005).
- [32] B. Roldan Cuenya, A. Naitabdi, J.R. Croy, et al., Phys. Rev. B 76, 195422 (2007).
- [33] S. Stankov, Y. Z. Yue, M. Miglierini, et al., Phys. Rev. Lett. 100, 235503 (2008).
- [34] B. Roldan Cuenya, W. Keune, et al., Phys. Rev. B 77, 165410 (2008).
- [35] B. Roldan Cuenya, J.R. Croy, L.K. Ono, et al., Phys. Rev. B 80, 125412 (2009).
- [36] B. Roldan Cuenya, L.K. Ono, J.R. Croy, et al., Appl. Phys. Lett. 95, 143103 (2009).
- [37] S. Stankov, M. Sladecek, T. Slezak, et al., J. Phys. Conf. Series 217, 012144 (2010).
- [38] S. Stankov, M. Miglierini, A. Chumakov, and I. Sergueev, Phys. Rev. B 82, 144301 (2010).
- [39] H.L. Smith, B.C. Hornbuckle, L. Mauger, et al., Acta Mater. 61, 7466 (2013).
- [40] Qi-C. Sun, D. Mazumdar, L. Yadgarov, et al., Nano Lett. 13, 2803 (2013).
- [41] S. De, K. Kunal and N.R. Aluru, J. Appl. Phys. 119, 114304 (2016).
- [42] R. Carles, P. Benzo, B. Pecassou and C. Bonafos, Scientific Reports 6, 39164 (2017);
- [43] D. Kivelson, H. Reiss, J. Phys. Chem. B **103** (1999).
- [44] J.C. Mauro, R.J. Loucks, S. Sen, J. Chem. Phys 133, 164503 (2010).
- [45] P.K. Gupta, J.C. Mauro, J. Chem. Phys 129, 067101 (2008).
- [46] H. Van Swygenhoven, D. Farkas, and A. Caro, Phys. Rev. B 62, 831 (2000).
- [47] M. Yuasa, T. Nakazawa, and M. Mabuchi, J. Phys.: Condens. Matter 24, 265703 (2012).
- [48] D. Olmsted, S.M. Foiles, and E.A. Holm, Acta Mater. 57, 3694 (2009).
- [49] N. Spiridis, M. Zajac, P. Piekarz, et al., Phys. Rev. Lett. 115, 186102 (2015).
- [50] D. Korn, A. Morsch, R. Birringer, et al., J. Physique 49, 769 (1988).
- [51] T.D. Shen, C.C. Koch, T.Y. Tsui and G.M. Pharr, J. Mater. Res. 10, 2892 (1995).
- [52] G.E. Fougere, L. Riester, M. Ferber, J.R. Weertman, R.W. Siegel, Mater. Sci. Eng. A 204, 1 (1995).
- [53] P.G. Sanders, J.A. Eastman, J.R. Weertman, Acta Materialia 45, 4019 (1997).
- [54] H.S. Cao, J.J. Hunsinger, and O. Elkedim, Scripta Materialia 46, 55 (2002).
- [55] H. Tanimoto, S. Sakai, E. Kita, H. Mizubayashi, Mater. Trans. 44, 94 (2003).
- [56] A. F. Yue, A. B. Papandrew, O. Delaire, B. Fultz, et al., Phys. Rev. Lett. 93, 205501 (2004).

- [57] R. Rohlsberger, W. Sturhahn, T.S. Toellner, et al.,J. Appl. Phys. 86, 584 (1999).
- [58] E.D. Hallman and B.N. Brockhouse, Can. J. Phys. 47, 1117 (1969).
- [59] T.G. Kollie and C.R. Brooks, Phys. Stat. Solidi 19, 545 (1973).
- [60] M.S. Lucas, L. Mauger, J.A. Muñoz, et al., J. Appl. Phys. 113, 17A308 (2013);
- [61] F. Körmann, A. Dick, T. Hickel, and J. Neugebauer, Phys. Rev. B 83, 165114 (2011).
- [62] O. Eriksson, J.M. Wills, and D. Wallace, Phys. Rev. B 46, 5221 (1992).
- [63] G.D. Samolyuk, L.K. Beland, G.M. Stocks, R.E. Stoller, J. Phys. Condens. Matter 28, 175501 (2016).
- [64] C.-W. Chen, Magnetism and Metallurgy of Soft Magnetic Materials, (Dover, New York, 1986) p. 105.
- [65] P.-Y. Li, Z.-H. Cao, X.-Y. Zhang, X.-L. Wu, Y.-N. Huang, and X.-K. Meng, Chin. Phys. Lett. 26, 036102 (2009).
- [66] P.Y. Li, H.M. Lu, Z.H. Cao, S.C. Tang, X.-K. Meng, X.S. Li, and Z.H. Jiang, Appl. Phys. Lett. 94, 213112 (2009):
- [67] H. M. Lu, P. Y. Li, Y. N. Huang, X. K. Meng, X. Y. Zhang, and Q. Liu, J. Appl. Phys. 105, 023516

- (2009);
- [68] S. Araujo-Barbosa and M.A. Morales J. Alloys Compds. 787, 935 (2019).
- [69] M. Palumbo, B. Burton, A. Costa e Silva, B. Fultz, et al., Phys. Stat. Solidi B 251, 1432 (2014);
- [70] A. Tschöpe and R. Birringer, Acta Metall. Mater. 41, 2791 (1993).
- [71] H. Ouyang, Ph.D. thesis in Materials Science, California Institute of Technology (Oct. 12, 1993). Download at https://thesis.library.caltech.edu/3304/
- [72] C.A. Kennedy, M. Stanescu, R. A. Marriott, and M.A. White, Cryogenics 47 (2007) 107.
- [73] P.D. Desai, Int. J. Thermophys. 8, 763 (1987).
- [74] T.G. Kollie, J.O. Scarborough, and D.L. McElroy, Phys. Rev. B 2, 2831 (1970).
- [75] N. W. Ashcroft and N.D. Mermin, *Solid State Physics* (Brooks/Cole, 1976).
- [76] S. Goldstein, Joel L. Lebowitz, Physica D 193 (2004)
- [77] D.C. Wallace, Statistical Physics of Crystals and Liquids (World Scientific, Singapore 2002). Chapter 19.